AIAA JOURNAL
Vol. 46, No. 6, June 2008

Dielectric Barrier Discharge Flow Control at Very Low Flight Reynolds Numbers

David Greenblatt*
Technion—Israel Institute of Technology, 32000 Haifa, Israel
Berkant Göksel† and Ingo Rechenberg‡
Electrofluidsystems Ltd., 13355 Berlin, Germany
and
Chan Yong Schüle,§ Daniel Romann,§ and Christian O. Paschereit¶
Berlin University of Technology, 10623 Berlin, Germany

DOI: 10.2514/1.33388

Experiments were performed on a flat-plate airfoil and an Eppler E338 airfoil at very low flight Reynolds numbers ($3000 \leq Re \leq 50,000$), in which dielectric barrier discharge plasma actuators were employed at the airfoil leading edges to effect flow control. The actuators were driven in a high-frequency (kilohertz) steady mode and a pulsed mode in which pulse frequency and duty cycle were varied in a systematic fashion. Optimum reduced frequencies for generating poststall lift were approximately between 0.4 and 1, and this was broadly consistent with zero-mass-flux slot-blowing data acquired at Reynolds numbers that were approximately 200 times higher. Nevertheless, profound differences in the response to reduced frequency and duty cycle were observed between the flat-plate and E338 airfoils. In general, actuation produced considerable performance improvements, including an increase in maximum lift coefficient of 0.4 to 0.8 and maintained elevated endurance at significantly higher lift coefficients. Actuation in the steady mode resulted in circulation control at $Re = 3000$. Pulsed actuation also exerted a significant effect on the wake at prestall angles of attack, in which control of the upper-surface flat-plate bubble shedding produced significant differences in wake spreading and vortex shedding. The flat plate was also tested in a semispan-wing configuration ($AR = 6$), and the effect of control was comparable with that observed on the airfoil.

Nomenclature

AR	=	aspect ratio
C_D	=	semispan drag coefficient
C_d	=	airfoil drag coefficient
C_L	=	semispan lift coefficient
C_l	=	airfoil lift coefficient
C_P	=	power coefficient
C_μ	=	mean momentum coefficient, $J/q_\infty c$
$\langle C_\mu \rangle$	=	oscillatory momentum coefficient, $\langle J \rangle / q_\infty c$
c	=	model chord length
DC	=	duty cycle
F^+	=	reduced excitation frequency, $f_m X_{\text{te}}/U_\infty$
f_c	=	plasma carrier frequency
f_m	=	modulation or pulsation frequency, $1/T_m$
J	=	time-mean actuator momentum
$\langle J \rangle$	=	oscillatory actuator momentum
m	=	mass
P	=	power
q_∞	=	freestream dynamic pressure
Re	=	Reynolds number based on chord length
s	=	wing semispan length, $b/2$
T_m	=	burst period, $1/f_m$
t	=	time
U_∞	=	freestream velocity
U, V, W	=	mean velocity components
u, v, w	=	instantaneous jet velocity components
X_{te}	=	distance from the actuator upper electrode to the trailing edge
x	=	coordinate measured from the upper electrode
x', y, z	=	coordinates measured from the model leading edge and center span
α	=	angle of attack
α_s	=	static stall angle

Subscripts

b	=	bin-averaged velocity
J	=	actuator jet
0	=	0-deg angle of attack
∞	=	freestream conditions

Superscripts

$\bar{u}$	=	time-mean component of u
$\tilde{u}$	=	coherent oscillatory component of u
u'	=	incoherent fluctuating component of u

Received 11 July 2007; revision received 11 December 2007; accepted for publication 15 December 2007.

*Senior Lecturer, Faculty of Mechanical Engineering, Technion City; davidg@technion.ac.il. Senior Member AIAA.
†Managing Director, 1 Volta Street; info@electrofluidsystems.com.
‡Emeritus Professor, Institute of Process Engineering, Department of Bionics, 71-76 Acker Street.
§Graduate Student, Institute of Fluid Dynamics and Engineering Acoustics, 8 Mueller-Breslau Street.
¶Professor, Institute of Fluid Dynamics and Engineering Acoustics, 8 Mueller-Breslau Street. Member AIAA.

I. Introduction

ACHIEVING sustained flight of micro air vehicles (MAVs) brings significant challenges due to their small dimensions and low flight speeds [1]. For so-called mini air vehicles, which operate in the $100,000 < Re < 300,000$ range, efficient systems can be designed by managing boundary-layer transition via passive tripping at multiple locations [2]. However, at Reynolds numbers routinely experienced by MAVs ($Re < 100,000$), conventional low-Reynolds-number airfoils perform poorly or generate no useful lift. Some of the best-performing airfoils in this Re range are cambered flat plates and airfoils with a thickness-to-chord ratio τ/c of

approximately 5% [1]. There are various definitions for MAV dimensions and weight, although one common definition refers to large ($b = 15$ cm and $m = 90$ g) and small ($b = 8$ cm and $m = 30$ g) MAVs [1]. To maximize wing area, these vehicles typically have low-aspect-ratio wings ($1 \leq AR \leq 2$) for which typical Reynolds numbers during loiter are in the range of $20,000 < Re < 80,000$, based on the aforementioned specifications. Innovative designs with larger-aspect-ratio wings, described in [2], can result in an even lower Reynolds number range.

The challenge of developing useful lift intensifies with yet smaller vehicles required to fly at even lower flight speeds [3]. This includes the development of so-called nano UAVs for which the missions include flying within confined areas. These are commonly termed nano air vehicles (NAVs) and are defined as weighing less than 10 g, with dimensions smaller than ~7.5 cm, and speeds between 0.5 and ~7.5 m/s [3]. The significant difficulty associated with generating lift at $Re < 20,000$ has led many to pursue biologically inspired approaches [4,5], in which the flight of small birds and insects is mimicked to a greater or lesser degree.

In contrast to these approaches, the objective of the present investigation is to study conventional active flow concepts on wings and airfoils at Reynolds numbers that are typical of small MAVs and NAVs ($3000 < Re < 80,000$). This was achieved using dielectric barrier discharge (DBD) actuators [6–8], typically driven in the 3- to 10-kHz frequency range, with low frequency pulsing. The actuators were extensively calibrated for both pulsed and nonpulsed (considered steady) actuation modes. This paper presents a summary based on several conference papers by the authors in which an Eppler E338 airfoil and a flat-plate airfoil were studied [9–15], and the two data sets are compared in detail. Smoke–wire experiments on the E338 airfoil revealed that the separation point is not fixed and moves upstream with increasing angle of attack from $x/c \sim 30\%$ at $\alpha = 0$ deg to the leading edge at $\alpha \sim 25$ deg [13]. This introduced an additional degree of complexity because the distance from the actuator to the separation point was not constant. Subsequent selection of the relatively simple flat-plate airfoil avoided this problem, thereby ensuring that the separation point would always be fixed at the leading edge and thus the relative position of separation to actuation would remain constant. An additional motivation for using this simple geometry and very-low-Reynolds-number range was to generate a data set that could be used to validate theoretical or computational approaches. Even though the introduction of camber improves baseline (uncontrolled) performance [1], it was not introduced in this investigation, to eliminate surface curvature as a parameter. Parametric studies, based on the measurement of aerodynamic loads, were carried out to establish the optimum reduced frequencies, minimum duty cycle (DC), and minimum power input required to maintain or maximize performance. Similar experiments were performed with the plate configured as a semispan wing of $AR = 6$.

The remainder of this paper is structured as follows. In Sec. II, a detailed actuator calibration is presented, Sec. III describes the experimental setup, and Sec. IV presents a detailed parametric study and airfoil comparison in which data are complimented with smoke–wire flow visualization.

II. Actuator Calibration

A. Background

The application of nonthermal plasma actuators to separation control is a relatively new technique, when compared with traditional boundary-layer control methods such as steady suction and blowing [16]. An excellent review of the their history, different actuator types, basic physics, mechanical effects, and flow control applications is provided in [17]. In recent years, particular attention has been focused on the asymmetric wall-mounted DBD configuration as a separation control actuator, precipitated by the initial demonstrations by Corke et al. [7] and Huang et al. [8]. The actuators are typically driven in the kilovolt range at several hundred hertz to several kilohertz. They produce plasma microdischarges at timescales $\mathcal{O}(10^{-9}$ s) during the positive- and negative-going drive signals [17,18]. The net result on the surrounding air is a steady wall jet with a peak velocity of less than 10 m/s, which is considered analogous to the jet blown from a two-dimensional slot. This somewhat limits conventional low-Reynolds-number applicability, because if the steady jet peak velocity does not exceed the freestream velocity, then performance can, in fact, be degraded [19].

Corke et al. [20] further advanced the application potential by driving the actuators in a pulsed mode; this technique was previously applied to zero-mass-flux piezoceramic actuators [21]. Pulsing the actuator brings with it two main advantages. First, the power supplied to the actuator can be significantly reduced because it is proportional to the DC. Second, periodic perturbations can achieve aerodynamic performance benefits that are comparable with or superior to steady blowing at one- to two-orders-of-magnitude less momentum input [22]. Corke et al. [20] demonstrated that both of these advantages can be realized and that the voltage required to reattach an otherwise separated flow was a minimum when the pulsed perturbations corresponded to $F^+ \sim 1$.

The direct analogy of a pulsed DBD actuator with zero-mass-flux blowing is an oversimplification because the actuator produces both a time-mean and an oscillatory velocity component and is thus analogous to a non-zero-mass-flux pulsed jet. The relative momentum produced by the time-mean and oscillatory components can have a profound effect on performance [22,23]. For example, the superposition of weak steady blowing or suction on a perturbation can have a deleterious or beneficial effect, respectively [22]. Superposition of large-amplitude blowing can have a positive effect [23].

B. Calibration Setup and Methods

With these considerations as background, a detailed calibration of the DBD actuator was undertaken; that is, the steady and oscillatory momentum components were measured directly. All measurements were performed in a quiescent environment ($U_\infty = 0$), as described next, in which close proximity to the actuator and wall were considered mandatory for a representative calibration. Three measurement techniques were considered: namely, particle image velocimetry (PIV), hot-wire anemometry, and two-dimensional laser Doppler anemometer (LDA). Hot-wire anemometry was eliminated based on uncertainty of the temperature near the actuator, the difficulty associated with very-low-velocity calibrations and zero crossings. Initial PIV data eliminated these problems, but reflections at $y \sim 0.5$ mm from the wall precluded accurate estimation of the full velocity profile and the maximum velocity very close to the actuator (also see [8]). Thus, the LDA was used henceforth for all calibrations. All data were acquired by closing the test section inlet and outlet and then seeding the enclosed volume using a commercial seed-particle generator (average diameter of 1 μm). In addition, flow visualization was performed by introducing a laser light sheet above the actuator, both perpendicular to and parallel to the electrodes.

All actuators employed in this study were of identical design [9–13]: namely, upper (exposed) and lower (encapsulated) electrodes (both 70 μm thick) separated by three layers of 50-μm-thick Kapton® tape (see Fig. 1). The trailing edge of the upper electrode and the leading edge of the encapsulated electrode were set at the same location ($x = 0$) and the latter was 10 mm wide. Measurements were performed at $x = 2.5$ and 5 mm downstream of the actuator in the ranges of 3 kHz $\leq f_c \leq$ 10 kHz and 6 $kV_{pp} \leq V \leq$ 10 kV_{pp}, and the majority of pulsed calibration was performed at $f_c = 4$ kHz. Pulsation frequencies were chosen to represent the F^+ range between $\mathcal{O}(0.1)$ and $\mathcal{O}(10)$, corresponding to 1 Hz $\leq f_m \leq$ 70 Hz, and the duty-cycle range tested was 1% $\leq$ DC $\leq$ 100%.

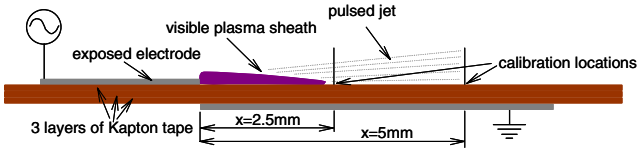

Fig. 1 Schematic of the DBD actuator used and calibration locations.

The pulsed-actuator calibrations presented in previous conference publications by the present authors [9–13] were found to be deficient in three respects. First, it was noted that after several minutes of use, the performance of the actuators degraded and finally stabilized. The degradation was accompanied by a discoloration of the glue used to bond the Kapton tape strips to one another as a result of dielectric heating. This indicated a change in the dielectric properties of the three-layered strip. Thus, calibrations performed before testing represented an overprediction of the momentum generated by the actuators. Consequently, all calibrations cited in this paper were based on measurements made after the airfoil load experiments. Second, for the previous calibrations, simple statistics were calculated directly from the LDA data. An examination of the time-resolved LDA velocity traces, however, illustrated that unacceptably large errors were being introduced due to velocity bias [24] and because the coherent and incoherent jet velocity components $\tilde{u}$ and u' were being lumped together [25]. Henceforth, pulsed LDA data were acquired in phase-locked mode, phase-averaged, and then the statistics were calculated based on the phase-averaged data. To achieve this, the velocity traces were subdivided into time bins δt (described in the next section) with $\delta t \ll 1/f_m$, and the random bursts detected within each time bin were simply averaged to yield $u_b(y,t)$ and $v_b(y,t)$. Third, the calibration was seen to vary significantly with distance downstream of the actuator. Hence, calibrations were based on a linear extrapolation to $x = 0$, based on measurements at $x = 2.5$ and 5 mm, respectively (see Fig. 1).

During the course of the measurements it was observed that the wall-normal velocities were relatively small ($|vb| \ll |ub|$), and they were henceforth not included in the calibration. Subsequently, the time mean and rms coherent velocity components were calculated according to

$$\bar{u}(y) = \frac{1}{T_m}\int_0^{T_m} u_b(y,t)\,\mathrm{d}t \tag{1}$$

and

$$\tilde{u}(y) = \left[\frac{1}{T_m}\int_0^{T_m} (u_b(y,t) - \bar{u}(y))^2\,\mathrm{d}t\right]^{1/2} \tag{2}$$

Finally, the total jet momentum was calculated using

$$J_{\mathrm{tot}} = J + \langle J\rangle = \int_0^\infty \rho\bar{u}^2\,\mathrm{d}y + \int_0^\infty \rho\tilde{u}^2\,\mathrm{d}y \tag{3}$$

where the first terms to the right of the equal signs represent the steady contribution and the second terms represent the oscillatory coherent contribution. The integration was carried out from the wall, to within ± 10 μm, until the mean velocity $\bar{u}$ zero crossing. The total momentum coefficient is defined as

$$C_{\mu,\mathrm{tot}} \equiv J_{\mathrm{tot}}/q_\infty c = C_\mu + \langle C_\mu\rangle \tag{4}$$

from Eq. (3) and is also sometimes expressed as $(C_\mu, \langle C_\mu\rangle)$ [22,23].

C. Calibration Results

To ensure a representative calibration, data were acquired as close to the actuator as possible. It was noted that when the LDA probe volume was placed within the plasma sheath (approximately $x < 2$ mm), no measurements were possible. When the probe was moved approximately 0.5 mm downstream of the visible plasma sheath, meaningful LDA data rates were achieved. Consequently, all cited calibration data were based on measurements between 2.5 and 5 mm downstream of the actuator upper electrode, as already described.

An example of data acquired and processed using the preceding techniques at a point close to the actuator and wall [$(x,y,z) = (2.5, 0, 0.45)$ mm, $f = 4$ kHz, $f_m = 5$ Hz, and DC = 20%] is shown in Fig. 2. Raw LDA data $u(y,t)$ for 200 cycles (crosses) are superimposed on the same time interval and the circles indicate bin-averaged values $u_b(y,t)$ within each δt. For purposes of illustration, the drive signal is initiated at $t = 30$ ms and terminated at $t = 70$ ms. The relatively small number of bins (20), corresponding to the large δt, was used here for illustrative purposes; this number was increased until the mean and coherent statistics converged. In general, 1000 time bins yielded adequate convergence of the $\bar{u}$ and $\tilde{u}$ statistics, calculated according to Eqs. (1) and (2), and illustrated in Fig. 3. Upon initiation of the drive signal, the velocity increases to its mean value, typically after less than 1 ms and appears to be turbulent; upon termination of the drive signal, the velocity decays asymptotically to zero, dropping to 10% of its mean value after approximately 20 ms. The apparent turbulence results from the 4-kHz oscillation, but the LDA data rates were not sufficiently high enough or regular enough to resolve this frequency. A comparison of statistics based on one bin with those based on 1000 bins clearly illustrates the large overprediction in the mean velocity $\bar{u}$ that would result by not accounting for velocity bias. The rms coherent component $\tilde{u}$ would be underpredicted by approximately 15%; this error would be introduced due to velocity bias and would not be significantly due to the lumping together of coherent and turbulent velocity components.

Time-mean and coherent velocity profiles [$\bar{u}(y)$ and $\tilde{u}(y)$] generated using the aforementioned techniques are shown in Figs. 4a and 4b. These data are for various modulation frequencies f_m and constant DC = 10%, but are representative of data at other duty cycles calibrated here. With increasing frequency, the peak mean velocity near the wall increases and the peak becomes more pronounced and tends toward the wall [at DC = 100%, the peak occurs at $z = 0.7$ mm (not shown)]; in contrast, the oscillatory component of velocity decreases with increasing f_m. These observations can be understood by considering the response of the flow shown in Fig. 2. As the pulsation frequency increases, the flow is reaccelerated to its peak value before it has fully decayed to zero. This results in the higher mean value with the corresponding lower

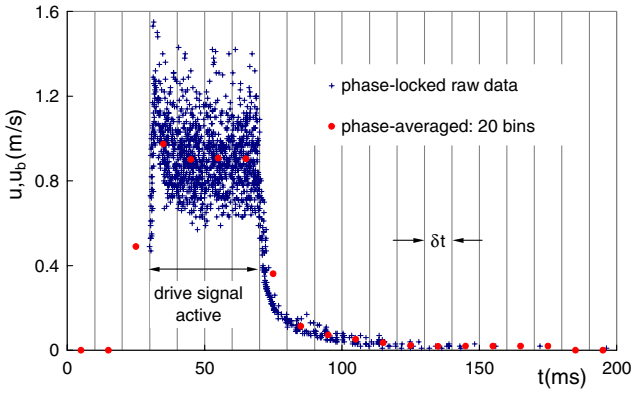

Fig. 2 Phase-locked raw LDA velocity data u with superimposed bin-averaged velocities u_b at $(x,y,z) = (2.5, 0, 0.45)$ mm and the conditions $f = 4$ kHz, $f_m = 5$ Hz, and DC = 20%.

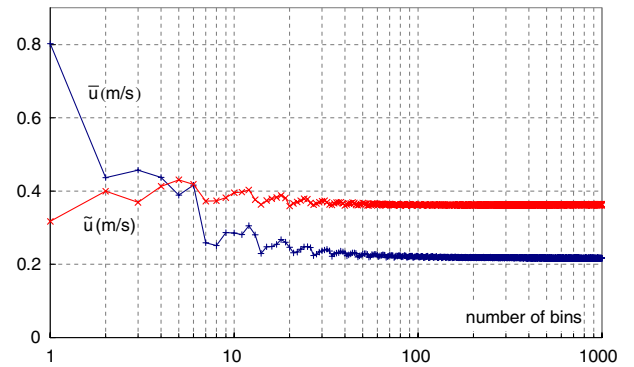

Fig. 3 Statistical convergence of the time-mean and coherent velocities, $\bar{u}$ and $\tilde{u}$, calculated according to Eqs. (1) and (2); data for 20 time bins correspond to those shown in Fig. 2.

coherent component. The coherent velocity profile also exhibits a double peak, with the largest peak consistently closer to the wall. The peak furthest from the wall is caused by a vortex that is generated above the actuator and was observed by means of laser-sheet/smoke flow visualization.

The resulting integration of the velocity profiles of the type shown in Figs. 4a and 4b, according to Eq. (3), are shown in Figs. 5 and 6 as a function of f_m and DC, respectively. The increase in mean velocity with frequency observed in Fig. 4a is reflected in the increased momentum J/ρ shown in Fig. 5. This effect saturates for $f_m > 10$ Hz. In contrast, the coherent momentum for $\langle J \rangle / \rho$ exhibits an optimum between 3 and 10 Hz and decreases for $f_m > 10$ Hz, as could be inferred from Fig. 4b. At low DC, both mean and oscillatory momentum increase dramatically (i.e., by more than two orders of magnitude), with a relatively small increase from DC = 1 to 4% (Fig. 6). For greater DC, the increase is relatively small, because both mean and oscillatory momentum increase by less than an order of magnitude for $5\% \leq \mathrm{DC} \leq 50\%$. The small but noticeable dip at DC = 6% is worth mentioning because its effect is manifested in the airfoil data to be presented in the next section. At DC = 100%, the momentum generated by the actuator is comparable with the lower-limit body-force estimate of [18] that is based purely on theoretical considerations.

To illustrate the applicability of the actuator shown in Fig. 1 for the present study, J and $\langle J \rangle$ ($f_m > 10$ Hz and DC = 10%) were nondimensionalized with respect to typical MAV and NAV dimensions, $c = 15$ and 5 cm, respectively. A U_∞ range was then selected to represent typical MAV and NAV Reynolds number ranges, and the results are shown in Figs. 7a and 7b for C_μ and $\langle C_\mu \rangle$ respectively. For the present example, J and $\langle J \rangle$ were close to the peak values (see Figs. 5 and 6). Moreover, it was observed that calibrations performed with $U_\infty > 0$ [10] resulted in even lower values. Thus, the ($C_\mu \langle C_\mu \rangle$) data presented here (Fig. 7) can be considered to be representative of the upper limit of the momentum coefficients achievable with these actuators.

On the abscissas, a demarcation between NAV and MAV Reynolds numbers is made, based on [1], and although this demarcation is somewhat subjective, it is employed here for illustrative purposes. On the ordinates, the approximate thresholds above which control becomes effective are shown for steady [16] and oscillatory control [22,23]. It is well known that a threshold for $\langle C_\mu \rangle$ can be two orders of magnitude less than that for C_μ, and this is reflected in Figs. 7a and 7b. For application to these low-Reynolds-number flows, the threshold values should be considered mainly as approximate indicators, because they are applicable to conventional low-Reynolds-number flows [22,23]. Figure 7a shows that in all cases, steady plasma jets do not cross the threshold for effective boundary-layer control for typical MAVs. Control may be marginal at around $Re = 20,000$. For NAV Reynolds numbers, steady boundary-layer control can only be expected for duty cycles of 100%. At very low Reynolds numbers, around $Re < 3000$, the C_μ available is comparable with that of circulation control at conventional low Reynolds numbers [16]. In contrast to steady actuation, oscillatory control can be expected to produce meaningful results at MAV Reynolds numbers, providing that the duty cycle is high enough. At NAV Reynolds numbers, duty cycles of 5% and greater can be expected to produce significant effects. Note that at this point, no attention has been paid to the power requirements of the actuation; these will be discussed in Sec. IV.

III. Airfoil Testing Setup

All airfoil load and flow-visualization measurements were conducted in an open-section wind tunnel of blowdown design with a 0.8- to 10-m/s velocity range. The test section dimensions were 400×280 mm and 600-mm diameter for the flat plate and E338, respectively. An aluminum, bending beam, strain-gauge-type balance (three-component) was designed and constructed for the measurement of forces and moments in the Reynolds number range of $3000 < Re < 200,000$. A variable-length sting was used to facilitate measurable forces corresponding to the large variation in load range. The flat plate and E338 airfoils (see the next section for the schematics) were mounted between oval and circular end plates, respectively. The balance was mounted above the wind tunnels and the airfoils were attached vertically to the balance by means of the sting.

Smoke–wire flow visualization of selected cases was performed by placing a stainless steel wire horizontally and under tension at one to two chord lengths upstream of each airfoil; recall that the models were mounted vertically. A mixture of paraffin oil and colored dye was applied evenly along the wire. The beading of the oil–dye mixture under surface tension was reasonably uniform, due to the horizontal mounting of the wire. A current was passed through the wire, and the resistive heating of the wire generated the streaklines that will be shown in Sec. IV. Illumination was applied from the rear of the airfoil so that a shadow would not be cast downstream of the airfoils. The streaklines were photographed using a digital camera using a simple mirror mounted directly under the airfoils. For all flow-visualization photographs, the lower end plates were removed. The photographs were taken randomly while the smoke was being generated, and for control cases, it was not locked to the phase of the control cycle. For all load measurements and flow-visualization photographs, a similar wind-tunnel velocity range U_∞ was employed.

The flat-plate airfoil was 2 mm thick with a 50-mm chord length and 150-mm span, made of plywood and covered with epoxy that

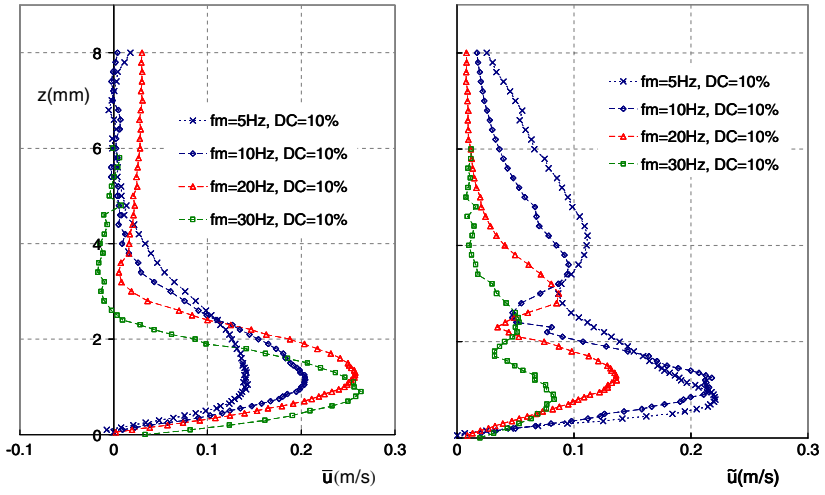

a) b)

Fig. 4 Velocity profiles for representative control frequencies at DC = 10% and $x = 5$ mm: a) mean and b) coherent.

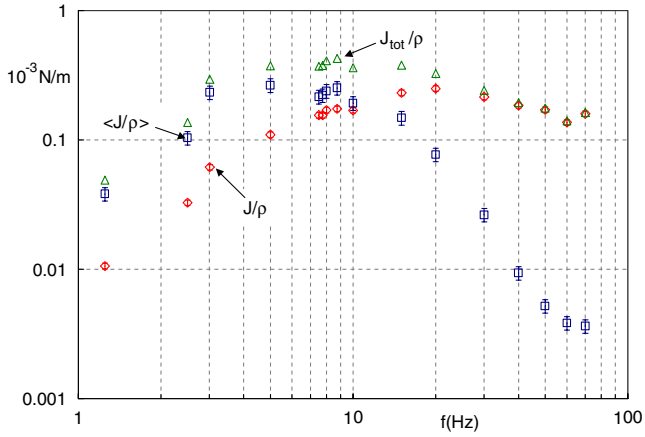

Fig. 5 Mean, oscillatory, and total momentum as functions of pulsation frequency at DC = 10%, 10 kVpp, and $f = 4$ kHz.

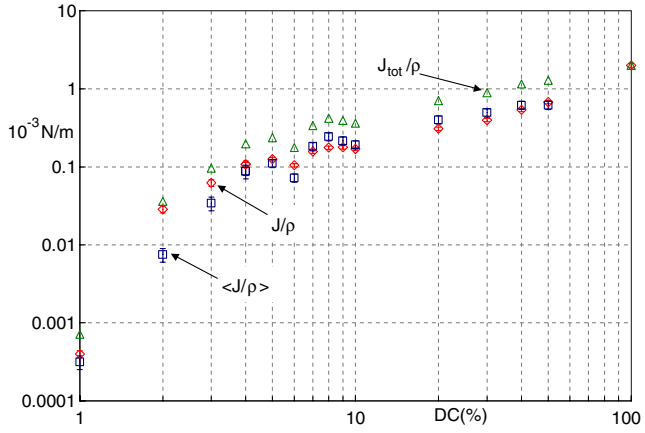

Fig. 6 Mean, oscillatory, and total momentum as functions of pulsation duty cycle at $f_m = 10$ Hz, 10 kVpp, and $f = 4$ kHz.

was sandpapered and polished. The leading edge was circular with a 1-mm radius, and the trailing edge was blunt (a previous investigation found very little effect of the trailing-edge design at low Reynolds numbers [1]). For 2D measurements, two end plates made from 1-mm-thick Plexiglas were fixed at both ends; for 3D measurements, the lower end plate was removed, producing $AR = 6$ (semispan $AR = 3$) [12]. The major source of error was a ±5-mg uncertainty associated with balance measurements. This resulted in lift and drag coefficient errors of $\Delta C_l = \Delta C_d \leq 0.013$ at $Re = 3000$ and $\Delta C_l = \Delta C_d \leq 0.003$ for $Re > 6000$. Long time averages, $tU_\infty/c > 400$, ensured negligibly small lift and drag coefficient precision errors $\mathcal{O}(0.001)$.

The flat-plate data set was compared with Eppler E338 data [10] that were acquired under similar conditions and flow-speed ranges. The original Eppler data [10] were augmented with additional load measurements and flow visualization under conditions identical to those already described [13]. The DBD plasma actuators were located at $x'/c = 2\%$ on both airfoils.

Baseline flat-plate data generated using the aforementioned setup were compared with the flat-plate wing data of Schmitz [26], which had a similar aspect ratio, and are shown in Figs. 8a and 8b. The C_l-vs-α slopes are similar, possibly due to the combined effect of higher Reynolds number and slightly smaller aspect ratio in the case of Schmitz. The zero-lift drag coefficient increases substantially with decreasing Reynolds numbers, mainly due to the increasing viscous component for which $C_D \sim Re^{-1/2}$.

IV. Discussion of Results

For a given application (in this case, performance enhancement at very low flight Reynolds numbers), a comprehensive optimization study should consider two separate, but related, aspects of the problem. The first has to do with strictly aerodynamic aspects (e.g., optimum actuator placement and optimum F^+ or minimum $\langle C_\mu \rangle$) and hence power, for which performance is maintained or improved. The second has to do with specifics of the actuator design, including electrodes and dielectric properties (thickness and dielectric coefficient) and the driving electronics used for generating the plasma. Here, attention must be paid to various power losses: for example, due to reactive power, dielectric heating, and plasma maintenance power [27]. In the present work, the aerodynamic aspects were mainly considered and actuator design aspects were not addressed. Consequently, no optimization studies were performed to reduce losses due to reactive power by impedance, matching the high-frequency power supply to the plasma actuator. The losses due to dielectric heating and maintenance power were kept to a minimum by driving the plasma with lower ionization frequencies that were still sufficient to ignite a glow discharge.

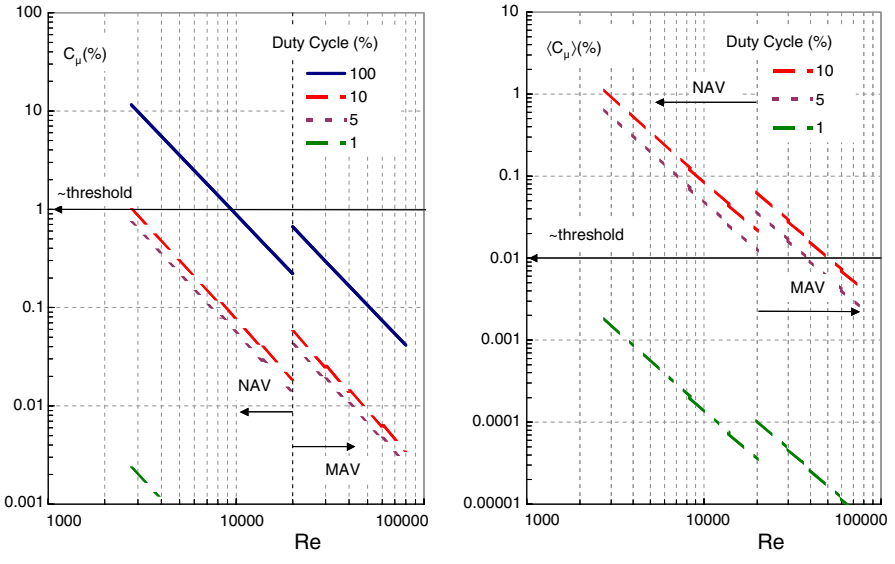

Fig. 7 Estimates of a) steady and b) oscillatory ($f_m > 10$ Hz and DC = 10%) components of the momentum coefficient based on DBD actuator calibration; assumed chord lengths of the MAV and NAV ranges are 15 and 5 cm, respectively.

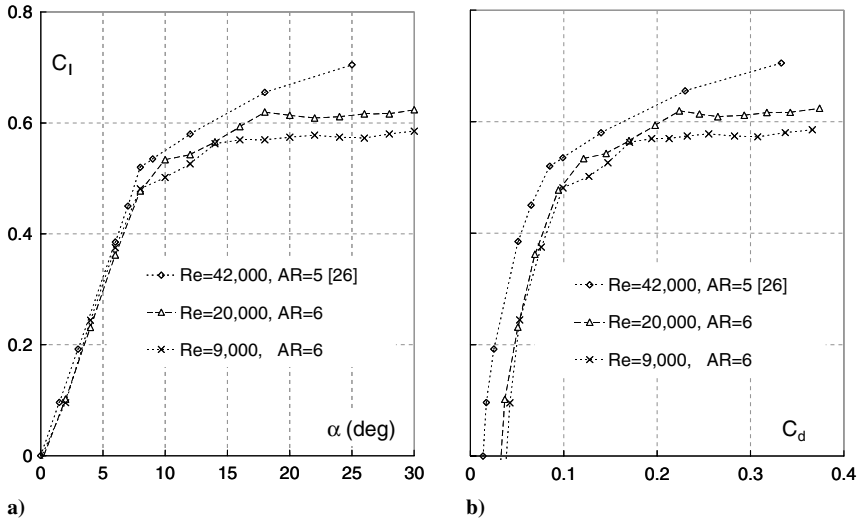

Fig. 8 Comparison of lift and drag coefficient data acquired on the semispan wing (lower end plate removed) with the wing data of Schmitz [24].

A. Reduced-Frequency Sensitivity

Corke et al. [20] observed, using pulsed plasma actuators, that the voltage (assumed proportional to $\langle C_\mu \rangle$) required to attach a poststall separated flow was a minimum when F^+ was slightly larger than one. Here, a systematic approach was adopted to determine the maximum poststall C_l as a function of reduced frequency at various poststall angles and Reynolds numbers (Fig. 9). The $\langle C_\mu \rangle$ values cited in the figure represent the maximum values in the associated frequency range. Selected representative smoke–wire visualization photographs are shown in Figs. 10a–10c. At all Reynolds numbers and $\alpha = 20\,\text{deg}$, a maximum in ΔC_l is evident at approximately $0.3 < F^+ < 0.6$; this is broadly consistent with zero-mass-flux blowing data acquired on a NACA 0015 at conventional low Reynolds numbers ($200,000 \le Re \le 600,000$) [22,23]. However, at lower α, the peak is not as clearly defined and extends to approximately one. For a given α, the C_l changes are slightly larger at the lower Reynolds numbers, which is due primarily to the relatively larger $\langle C_\mu \rangle$ introduced by the actuator. Nevertheless, once a threshold momentum input is exceeded (i.e., $\langle C_\mu \rangle \sim 0.14\%$ at $Re = 9000$) an order-of-magnitude increase (i.e., $\langle C_\mu \rangle \sim 1.2\%$ at $Re = 3000$) has a relatively small effect, increasing ΔC_l by only an additional 25%. This result is fully consistent with data acquired at conventional low Reynolds numbers for which perturbations were supplied by means of zero-mass-flux blowing [28].

Flow visualization of the baseline case (Fig. 10a) clearly shows separation from the leading edge and subsequent rollup of the shear layer into distinct vortices. Flow separation from the trailing edge appears to generate vortical structures with a longer wavelength. The difference between the flow over the stalled airfoil and control at $F^+ = 0.42$ is clearly seen by comparing Figs. 10a and 10b. With control, the separated shear layer that detaches from the leading edge rolls up into a vortex (or bubble) that attaches to the airfoil surface. Downstream of this vortex, the previously generated vortex is in the process of being shed into the wake. A clockwise trailing-edge vortex can also be seen that arises as a result of the low pressure now present on the plate's upper surface. It is believed that the strong adverse pressure gradient existing on the upper surface of the airfoil is responsible for the dramatic upward distortion of the streamlines. Increases in control frequency produce rolled-up vortices successively closer to the leading edge. For example, an increase in frequency by a factor of 5, to $F^+ = 2.1$ (Fig. 10c), is only effective at transporting momentum toward the airfoil surface at $x/c < 0.1$. Immediately downstream of this, the small vortices are not effective at transporting high momentum fluid to the surface. Control at $F^+ < 0.1$ resulted in large lift and drag oscillations, and the data

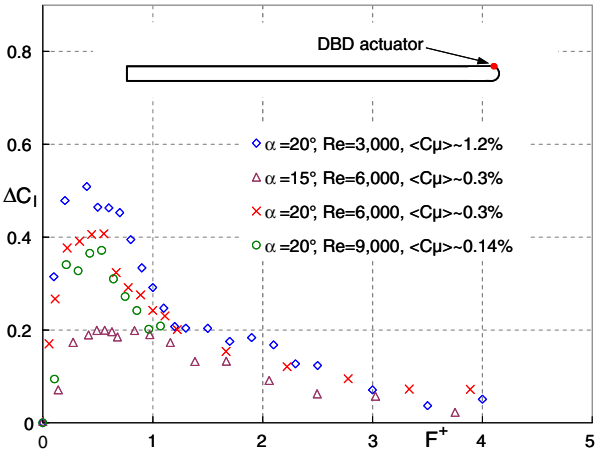

Fig. 9 Poststall frequency scan at very low flight Reynolds numbers on the flat-plate airfoil. Plasma is driven at 10 kV_{pp}, $f = 4$ kHz, and DC = 5%. The maximum oscillatory momentum coefficient is indicated as $C_{\mu,\max} < 1\%$. The inset shows the airfoil schematic in which flow is from right to left.

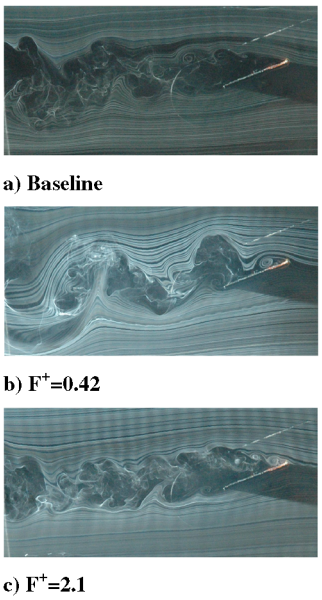

a) Baseline

b) F^+=0.42

c) F^+=2.1

Fig. 10 Smoke-visualization photographs on the flat-plate airfoil corresponding to a) baseline state, b) optimum control, and c) nonoptimum control at $Re = 3000$, $\alpha = 20\,\text{deg}$, and control DC = 5% (cf. Fig. 9).

shown in Fig. 9 represent long time averages ($tU_\infty/c > 400$). These observations are consistent with the generation of a leading-edge vortex that is shed into the wake before the following vortex is generated [29]. Lift oscillations are dramatically reduced when at least two vortices are present on the airfoil surface at any instant. Similar experiments were performed by driving the plasma actuators at 5 kHz and the aerodynamic results did not change materially. Observations that are common to both the present observations and to those associated with biological flight at comparable Reynolds numbers are discussed in Sec. IV.C.

It is instructive to compare the present data set with that acquired under similar conditions on the E338 airfoil [10,13] at $20,500 \leq Re \leq 50,000$ (poststall $\alpha = 14$ and 18 deg) and employing 3 and 5% duty cycles (Fig. 11). At all reduced frequencies considered, there was a significantly larger positive effect on poststall C_l. At the higher angle of attack ($\alpha = 18$ deg), the lift variation with frequency was mild, although an optimum was observed at $F^+ \approx 1.2$. Nevertheless, even at $F^+ \approx 10$, significant effects were observed, and this is totally contrary to the flat-plate observation in which improvements were inconsequential for $F^+ > 3$ (cf. Figs. 9 and 11; note the same vertical scale). Moreover, at the lower angle ($\alpha = 14$ deg), the frequency dependency was more pronounced, and this observation was again at odds with those of the flat plate.

Poststall flow-visualization photographs for the E338 baseline and controlled scenarios (Figs. 12a and 12b, respectively), when compared with the corresponding flat-plate-airfoil photographs (Figs. 10a and 10b, respectively), illustrate important differences between the two airfoils. (The actuator ground wire is visible in the photographs.) With regard to the baseline state (cf. Figs. 10a and 12a), it was noted that separation occurs at approximately $x/c = 10\%$ on the E338, and the separation streamlines are closer to the airfoil surface than in the case of the flat plate. Also, the rollup of vortices observed at the leading edge of the plate without control is absent on the E338, and this was also observed using flow visualization at $Re = 10,000$ and 6000. With perturbations introduced upstream of separation ($x/c = 2\%$), the vortex generated has a larger aspect ratio; that is, it is closer to the airfoil surface and is not as clearly defined as that on the flat plate (Fig. 10b). Thus, control in this case is more effective at turning the streamlines toward the airfoil surface, and this results in larger lift changes. In addition, the dramatic upward distortion of the streamlines near the flat-plate trailing edge, associated with the downstream vortex, is not evident on the E338. It is a combination of these factors that leads to higher lift coefficients generated on this airfoil (cf. Figs. 9 and 11). It is clear that details of the leading-edge geometry have a major effect on the efficacy and optimum frequency range of active flow control at very low flight Reynolds numbers.

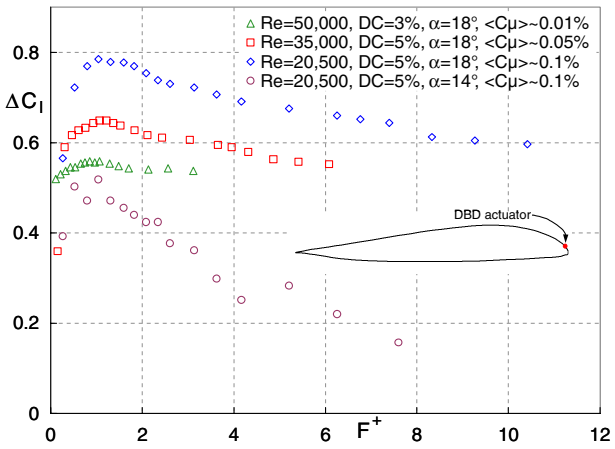

Fig. 11 Poststall frequency scan on the Eppler E338 airfoil at low flight Reynolds numbers [13]. The inset shows the airfoil schematic in which flow is from right to left.

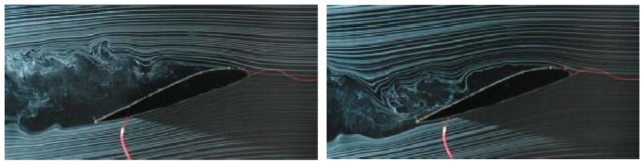

a) Baseline **b) Control**

Fig. 12 Smoke-visualization photographs on the E338 airfoil corresponding to a) baseline state and b) optimum control ($F^+ = 1.0$ and DC = 5%); $Re = 20,000$ and $\alpha = 18$ deg (cf. Fig. 11) [13].

B. Duty-Cycle Dependence

As described in Sec. II, wave modulation was employed such that the 4-kHz carrier wave was modulated by a square wave corresponding to low frequencies appropriate for separation control (cf. [22]). Thus, the duty cycle was varied by changing the fraction of the square-wave period that the actuator was activated, and this is expressed as a percentage. DC variations are shown in Fig. 13 in which data were acquired corresponding to the optimum reduced frequencies. All data, independent of α or Reynolds number, show a relatively rapid increase in C_l with DC. At a large DC, the effect on lift is small, with perhaps a gradual decrease as DC is increased beyond 10%. Figures 6 and 7 provide an explanation for these observations. At $Re < 30,000$ and DC = 5%, the oscillatory component of momentum lies mainly above the threshold necessary for control (Fig. 7b). This explains the positive effect observed on lift irrespective of the DC. The increase from DC = 1 to 5% (Fig. 6) results in a more than two-order-of-magnitude increase in actuator momentum, and this is primarily responsible for the larger increase in C_l observed here. An increase from DC = 5 to 10% does not bring about a significant difference in $\langle J \rangle$, and this is reflected in the small increase in C_l for this range. Note, in addition, that the small reduction in C_l at DC = 6% (Fig. 13) is fully consistent with the actuator calibration shown in Fig. 6. The increases in the steady-momentum component are below the threshold and thus it can be assumed that they play only a minor role (Fig. 7a). Substantial increases in DC may result in the threshold being exceeded, but C_μ is still too small to have a negative impact on performance. There may be a slight deleterious effect (e.g., DC $\rightarrow$ 50%) due to relatively low near-wall momentum (Fig. 7a), which acts to promote boundary-layer separation (cf. [19,22,23]).

The flow-visualization photographs shown in Figs. 10a–10c, 14a, and 14b add a qualitative dimension to these measurements. At DC = 0.33%, a small effect can be observed as the streamlines are deflected toward the plate upper surface (Figs. 14a). However, there is no clear evidence of the formation of a leading-edge vortex. With an increase to DC = 5 and 50%, a leading-edge vortex is clearly evident (Figs. 10b and 14b).

Data acquired on the E338, close to its optimum reduced frequency ($F^+ = 1$), showed some generic similarities but also some very profound differences when compared with the flat plate

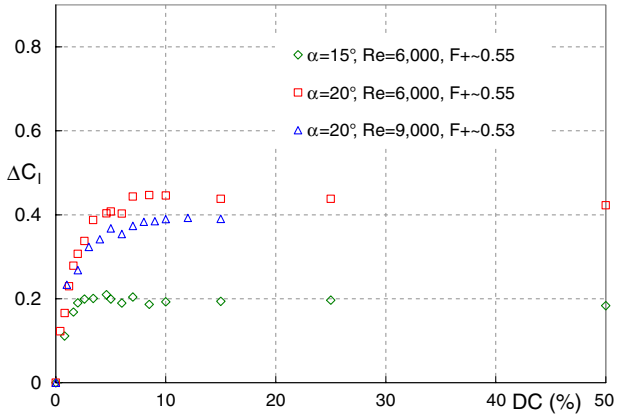

Fig. 13 Flat-plate poststall lift coefficient variation as a function of duty cycle.

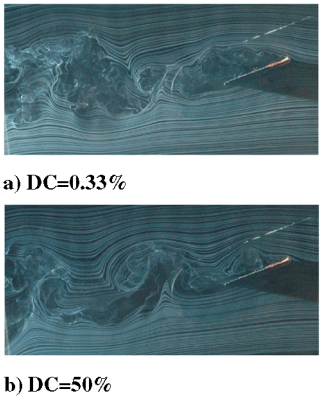

a) DC=0.33%

b) DC=50%

Fig. 14 Flat-plate flow visualization at $F^+ = 0.46$ for varying duty cycles (indicated) with $Re = 6000$ and $\alpha = 20$ deg.

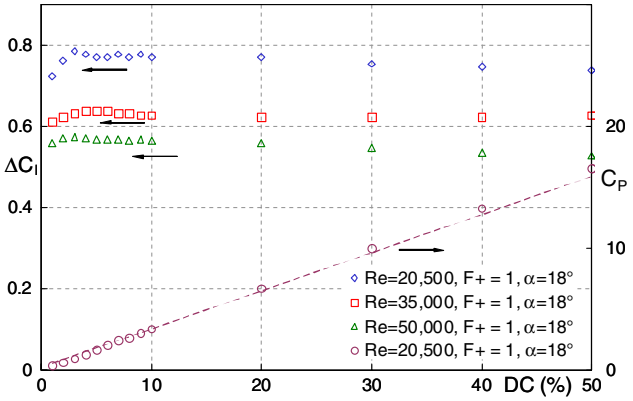

Fig. 15 Poststall lift coefficient variation as a function of duty cycle on the Eppler E338 airfoil [13]. Change in the lift coefficient is shown on the left ordinate; the power coefficient is shown on the right ordinate.

(cf. Figs. 13 and 15). A mild optimum was observed in the approximate range $2\% < \mathrm{DC} < 8\%$; as in the case of the flat plate, this is consistent with increases to the oscillatory momentum. However, the difference between the lift generated at optimum and nonoptimum duty cycles differed by a small amount: namely, $\Delta C_{l,\max} < 0.1$ as $\mathrm{DC} \to 0$. Figure 15 also shows the measured power, expressed as the power coefficient $C_P \equiv P/\frac{1}{2}\rho U_\infty^3 c$ input to the actuator and emphasizes the important observation that similar performance benefits can be attained at a fraction of the power. With the power consumption reduced to 1.2 mW/cm (0.66% duty cycle) $C_{l,\max}$ did not drop significantly. At these duty cycles, however, the actuators could not be reliably calibrated and were estimated to produce $\langle C_\mu \rangle \sim 0.001\%$. Note that this is considered to be below the thresholds typically required for effective separation control at conventional low Reynolds numbers. Flow visualization of the baseline and control cases for various representative duty cycles (1, 5, and 50%) showed that the basic vortex generation and advection over the airfoil surface were similar [13]. These similarities are, in essence, fully consistent with the small lift coefficient changes reflected in Fig. 15.

C. Performance Indicators and Control Mechanism

1. *Flat-Plate Data*

C_l-vs-α and C_l-vs-$C_d + C_{\mu,\mathrm{tot}}$ polar plots are shown in Figs. 16a–16d, indicating the effect of control at four Reynolds numbers. In each instance, control is applied in the range that produced optimum poststall C_l: namely, $0.4 < F^+ < 0.6$. For illustrative purposes, the data are discussed with respect to $Re = 3000$, and the corresponding description is provided with reference to flow visualization shown in Figs. 17a–17f. A similar description applies at the higher Reynolds numbers, with the exception of the relative magnitudes of C_{d0} and $C_{\mu,\mathrm{tot}}$. At $Re = 3000$, $C_{\mu,\mathrm{tot}} \approx 0.5 C_{d0}$, but for $Re \geq 6000$, $C_{\mu,\mathrm{tot}} \ll C_{d0}$, and its inclusion in subsequent definitions has a negligible effect on the data. At prestall angles of attack, typically $\alpha < 10$ deg, control results in a reduction in lift. This is because the long bubble that exists naturally on the plate's upper side is reduced or eliminated as a result of the perturbations. This can be seen in the flow-visualization photographs at $\alpha = 6$ deg (discussed later). With increasing α, the bubble cannot close on the plate surface and bursts (Fig. 17a). Control is seen to produce a long, relatively high-aspect ratio bubble on the upper surface, but no significant effects are seen on the wing lift or drag (Fig. 17b). Further increases in angle of attack ($\alpha = 14$ deg) result in complete separation from the upper surface, accompanied by a significant drag rise (Fig. 17c). Control encloses a bubble near the leading edge with an accompanying increase in lift and reduction in drag. The bubble is shed downstream, and before it leaves the airfoil surface, a new bubble is generated near the leading edge (Fig. 17d). In the vicinity of $C_{l,\max}$ ($\alpha \sim 20$ deg), the same control mechanism is observed, but the preceding vortex, which has traveled down the airfoil chord, is accompanied by significant deviation of the streamlines, indicating trailing-edge separation (Fig. 10b). In deep poststall ($\alpha = 24$ deg), control still produces the leading-edge vortex, but trailing-edge separation (Fig. 17f) results in a loss of lift and an increase in drag.

It is well known that small flying creatures, for which the wings generate useful lift at these Reynolds numbers, remain airborne by means of at least one unsteady flow mechanism [30–33]. One such mechanism is the so-called separation bubble or vortex, which forms during the downstroke of the wing and generates the high lift required for flight. This bubble is similar to the well-known dynamic stall vortex (DSV) that is observed on oscillating airfoils. Control of the DSV has received considerable attention due to its association with dynamic stall on rotor blades and wind turbines [29]. The apparent paradox that the DSV generates very large oscillations in lift but is at least partially responsible for the flight for small creatures can be resolved as follows. From the statistical data summarized by [30], for the NAV range, the typical reduced frequencies associated with wing flapping are $0.1 \leq F^+ \leq 1$ (in hover $F^+ \to \infty$). This should be contrasted with equivalent reduced frequencies associated with oscillating helicopter rotor blades: namely, $0.015 \leq F^+ \leq 0.05$. Thus, some flying creatures can generate dynamic stall vortices at a rate high enough to ensure sustained flight; that is, at least one vortex will always be present on the upper surface of the wing or body at any instant [23]. A similar explanation can be given for active flow control introduced here, in which there are typically two vortices present on the airfoil at any instant. This ensures stable, as well as effective, lift because the excitation-generated vortices do not bring about large variations in aerodynamic loads [34].

The aforementioned performance improvements result in modest gains to the airfoil efficiency parameter [35] $C_l/(C_d + C_{\mu,\mathrm{tot}})$ (Figs. 18a and 19a). The low efficiency throughout the α range for both baseline and control scenarios is a consequence of the high viscous drag associated with low Reynolds numbers and of the large upper-surface bubble. These sources of drag may be unavoidable at these low Reynolds numbers. Somewhat better results are obtained by the endurance parameter [35] $C_l^{1.5}/(C_d + C_{\mu,\mathrm{tot}})$ (Figs. 18b and 19b). Here, the same or greater endurance can be achieved at up to two times the lift coefficient. This is of importance for mission-critical loitering flight in which a combination of low flight speeds (high C_l) and high endurance is often desirable. As expected, there is an increase in both baseline and control efficiency and endurance parameters with increasing Reynolds number (cf. Figs. 18a and 19a).

Removal of the lower end plate produced a semispan wing with $AR = 6$, discussed previously with reference to the data presented in Fig. 8. A comparison of the efficiency parameter for the two-dimensional configuration and the semispan configurations (Figs. 19a and 19b) shows, as expected, that the baseline $[C_l/(C_d + C_{\mu,\mathrm{tot}})]_{\max}$ exceeds $[C_L/(C_D + C_{\mu,\mathrm{tot}})]_{\max}$ due to induced drag. However, the same indicators associated with control do not show this trend and there is even a small increase on the finite wing. Similar observations can be made with respect to $C_l^{1.5}/(C_d + C_{\mu,\mathrm{tot}})$ and

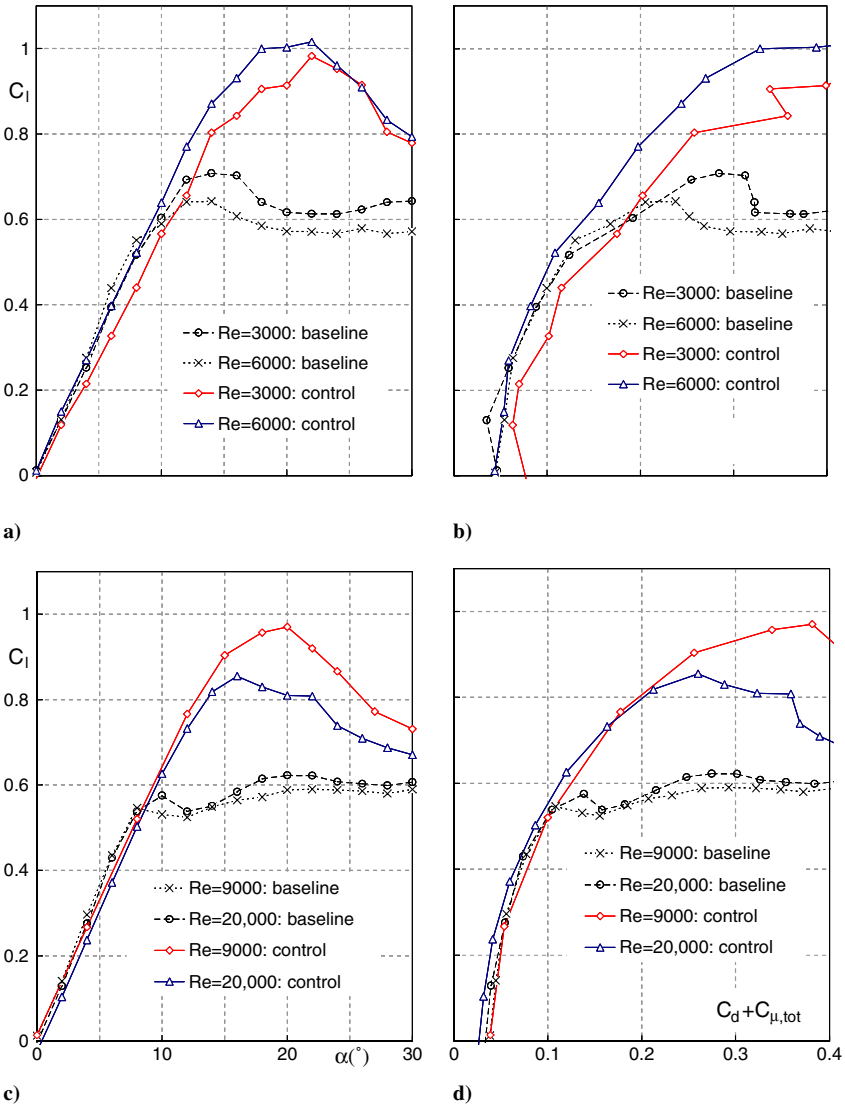

Fig. 16 Effect of control on the flat-plate-airfoil performance at typical NAV Reynolds numbers; control is at $0.4 < F^+ < 0.6$ and DC = 5%.

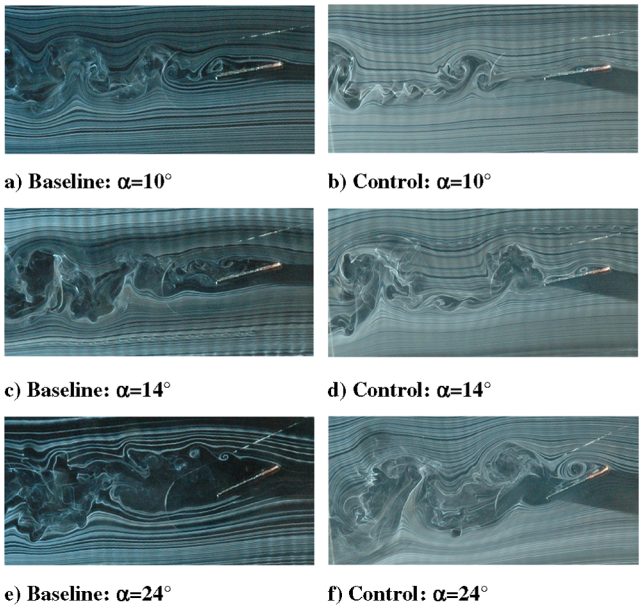

Fig. 17 Flow visualization of baseline and optimum control at $F^+ = 0.42$ and DC = 5% at $Re = 3000$ for increasing angle of attack.

$C_L^{1.5}/(C_D + C_{\mu,\text{tot}})$ (cf. Figs. 19c and 19d). It has been noted previously that actuation along the entire leading edge reduces separation associated with the wingtip vortex [36], and this is the most likely explanation for the increased efficiency and endurance parameters observed here.

2. *Eppler E338 Data*

The weak sensitivity to duty cycle, and therefore power input, on the E338 prompted further optimization attempts by studying the effect of input voltage on the C_l-vs-α performance at $Re = 20,500$ [low end of the MAV Reynolds number range (Fig. 7b)]. It was determined that for $V = 10$ kVpp, $F^+ = 1$ and DC = 3% (corresponding to $P = 5$ mW/cm; $\langle C_\mu \rangle = 0.05\%$), the effect on the airfoil performance was clearly significant (Fig. 20a) and $C_{l,\max}$ was larger than at higher Reynolds numbers [10]. All data were generated for increasing α (filled symbols) and decreasing α (open symbols).

At lower actuator driving voltages (8 kVpp) corresponding to 4 mW/cm and $\langle C_\mu \rangle = 0.04\%$, the C_l-vs- curve exhibited a definite nonlinearity between 10 and 15 deg. The airfoil appears to stall, but with increasing α it once again begins to generate lift. Nevertheless, this nonlinear behavior has very little impact on $C_{l,\max}$. It is of particular interest to note that this nonlinear feature does not suffer from any significant hysteresis, because the data show the same trend irrespective of whether α is increasing or decreasing (Fig. 20a). Similar observations were also made by O'Meara and Mueller [37]

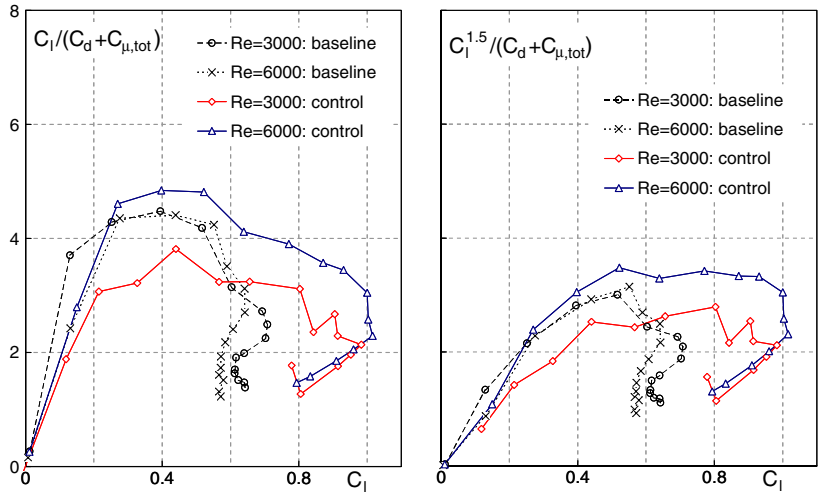

a) **b)**

Fig. 18 Parameters for the flat-plate airfoil: a) efficiency and b) endurance; control is at $F^+ \sim 0.4$ and DC = 5%.

on uncontrolled airfoils at $Re \sim 45,000$, and they attributed the nonlinear behavior to a separation bubble on the upper surface. Apparently, a longer bubble is associated with a decrease in the lift-curve slope. The similarity between the nonlinear behavior observed here in the presence of control and that observed in [37] suggests that the same mechanism is active in both cases. Nevertheless, time-resolved flowfield measurements would be required to properly resolve this question.

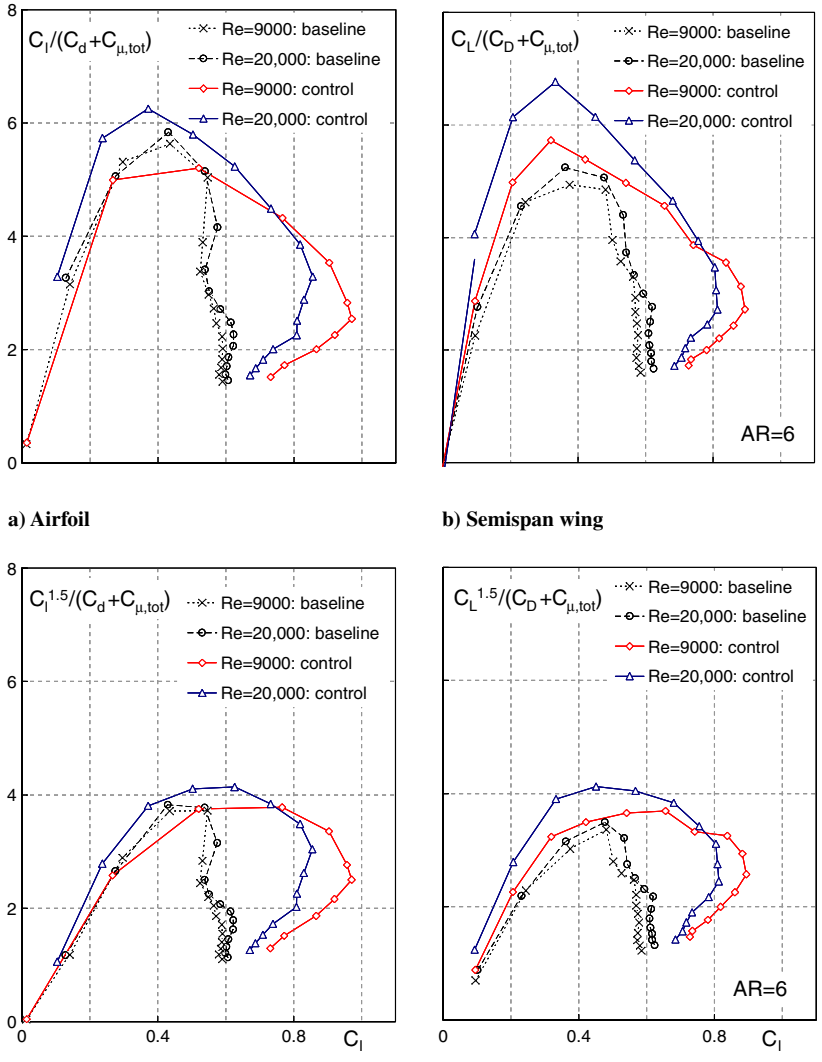

a) Airfoil **b) Semispan wing**

c) Airfoil **d) Semispan wing**

Fig. 19 Flat-plate efficiency and endurance parameters; control is at $0.4 < F^+ < 0.6$ and DC = 5%.

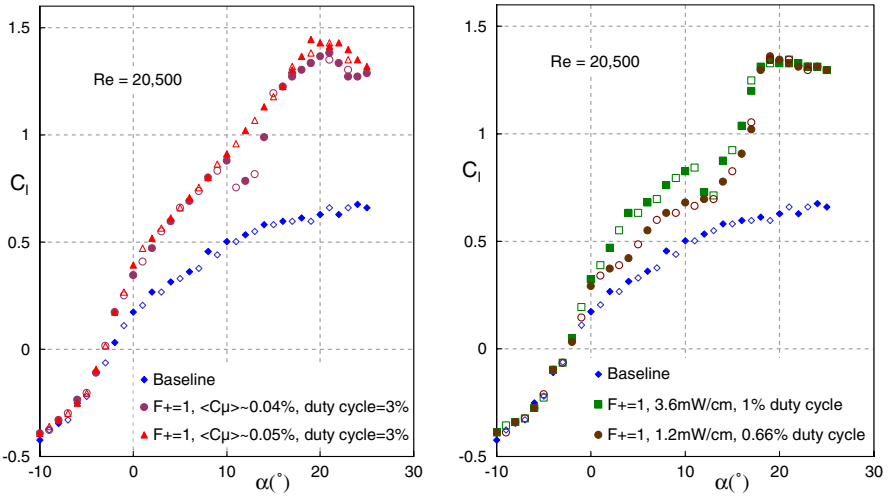

Fig. 20 Effect of duty-cycle reduction and peak-voltage reduction (10–8 kVpp) on E338 airfoil performance at low MAV Reynolds numbers: a) DC = 3% and b) DC = 1 and 0.66%; α increasing (filled symbols) and α decreasing (open symbols).

Finally, an effort was made to reduce the duty cycle even further while maintaining $C_{l,\max}$. Figure 20b shows results for simultaneously reducing the DC from 1 to 0.66% duty cycles and reducing the input voltages from 10 to 8 kVpp, respectively. This corresponds to a reduction in C_P from 5.9 to 2.0. In all cases, the excitation frequency was 10 Hz, corresponding to a reduced frequency $F^+ = 1$. For these data, the relative momentum input was extremely low ($\langle C_\mu \rangle \sim \mathcal{O}(0.01)\%$) (see Fig. 7b), and thus it was deemed more meaningful to also present the results in terms of milliwatts per centimeter, as shown in Fig. 20b. It is clear that the lift slope remains highly nonlinear, but at the lowest power input, namely 1.2 mW/cm, there was not a meaningful reduction in $C_{l,\max}$. In fact, the lift slope then appeared similar to the baseline higher Reynolds number data of [1]. Figures 21 and 22 show flow-visualization photographs that correspond to the C_l data shown in Fig. 20b. It can be clearly seen from Fig. 21 (left-hand column) that the baseline separation point moves upstream with increasing angle, with separation at $x'/c \approx 0.2$ at $\alpha = 10$ deg (Fig. 21a) and close to the leading edge $\alpha = 25$ deg (Fig. 21e). When control is applied far upstream of separation (cf. Figs. 21a and 21b), the effect is relatively small, as also seen in Fig. 20b. However, at higher angles of attack when separation occurs near the leading edge (Figs. 21c and 21e), the basic mechanism of control does not depend strongly on angle of attack. Furthermore, the vortex generation and advection mechanism present at DC > 1% [13] remains active as the duty cycle is successively decreased to as low as 0.66%, as shown in Fig. 22.

In dimensionless terms, the minimum C_P achieved here is approximately 650 times larger than that required at $Re = 140,000$, and the C_μ differs by an order of magnitude (see [10]). Note, however, that the differences in performance are not comparable: at $Re = 140,000$, $C_{l,\max}$ increases by 0.06 (comparable with [20]), whereas at $Re = 20,500$, an airfoil that otherwise does not generate useful lift achieves better performance than at conventional low Reynolds numbers.

Further optimization studies were not conducted, and an exhaustive range of high-frequency actuation was not attempted. However, similar experiments were performed by driving the plasma actuators at 5-kHz-and-higher frequencies. Similar aerodynamic results (not shown) were obtained, but it was noted that with increasing plasma frequency at constant voltage, the power consumption increased. This was assumed to be due to dielectric heating [27]. Frequencies lower than 4 kHz were also not employed, due to insufficient cycles present when pulse modulation was introduced in the hertz range with low duty cycles.

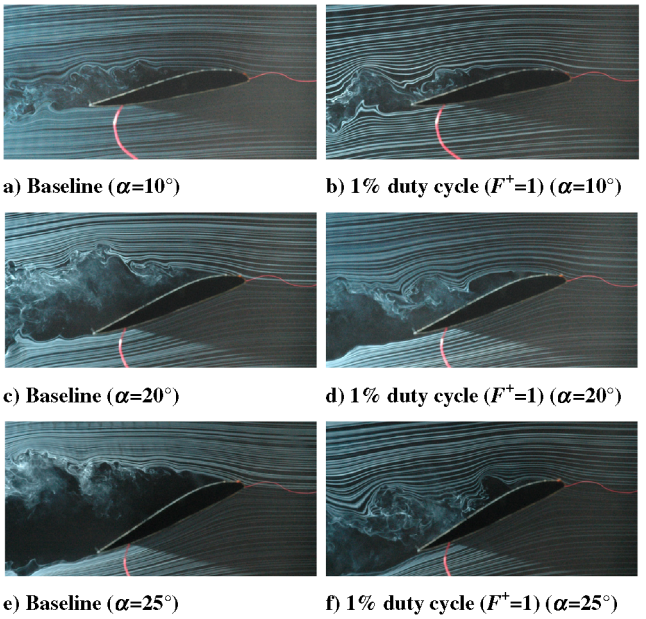

Fig. 21 Smoke–wire flow visualizations showing the effect of plasma actuation at $\alpha = 10, 20$, and 25 deg with 10 kVpp (4 kHz) at $Re = 20,500$; $\langle C_\mu \rangle \approx 0.01\%$, and DC = 1%; baseline (left) and control (right).

D. Steady Control: 100% Duty Cycle

Historically, steady slot blowing was employed as an effective means of boundary-layer control, but it was abandoned, mainly due to design complexity and heavy plumbing systems [16]. At very low flight Reynolds numbers, an analogy to steady blowing can be achieved using DBD actuators, in which the actuators are not pulsed: that is, are driven at DC = 100%. It is generally assumed that the

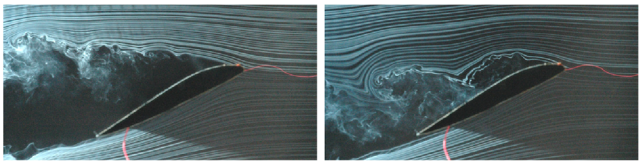

Fig. 22 Smoke–wire flow visualizations showing the effect of plasma actuation at $\alpha = 25$ deg with 8 kVpp at $Re = 20,500$; $\langle C_\mu \rangle < 0.01\%$.

flow does not respond to the high-frequency oscillations (presently 4 kHz), and the flow can be considered as a steady jet. Returning to Fig. 7a and considering the momentum coefficient calibration for DC = 100%, it is evident that steady control may only be applicable in the extremely low flight Reynolds number range: namely, $Re < 10,000$. Attempts were made to measure the lift and drag forces, but the combination of high instrumentation sensitivity and strong electromagnetic radiation produced by the actuator resulted in unacceptably high noise levels, thereby precluding meaningful measurements. Thus, only smoke–wire flow visualization was performed at these Reynolds numbers to provide a qualitative description of the flow.

Baseline and control photographs at several poststall angles are shown in Figs. 23a–23h for $Re = 3000$. Based on the calibration shown in Fig. 7a, it was assumed that steady control produces thrust at low α because $C_{d0} = 0.044$, whereas control produces $C_\mu \approx 0.1$, although this was not directly verified by means of a wake survey. At the poststall angles shown in the figures, it is clear that steady blowing dramatically eliminates separation by producing a high-speed jet adjacent to the surface. This can be achieved up to $\alpha = 26$ deg. The stall mechanism at $\alpha > 26$ deg is similar to that already described. Similar flow patterns were observed on the E338, but are not shown here.

A comparison of the streamlines generated by steady blowing with those of a potential flow about a flat plate are shown in Figs. 24a and 24b. Details of the visualized streamlines, particularly in the leading-edge region, correspond well with potential flow theory. However, the upper-surface flow is seen to separate at approximately $x/c = 20\%$, and the separated region grows to a substantial fraction of the chord length. Based on extrapolation of the experimental data (not shown), it should not be expected that $C_{l,\max}$ will exceed 1.6 at $\alpha = 26$ deg.

E. Control of the Flat-Plate Airfoil Wake

At prestall angles of attack, it was observed that α has a significant effect on the wake stability and structure. At $\alpha = 0$ deg, the flow on both surfaces separates at the blunt trailing edge and the streamlines smoothly merge at approximately $x/c = 10\%$ downstream of the trailing edge. The wake is seen to undergo an instability downstream of the trailing edge that evolves into a series of alternately signed vortices, similar to a Kármán vortex street observed immediately downstream of bluff bodies (Fig. 25a). If it is assumed that the vortices' velocity is $\mathcal{O}(U_\infty)$, then this corresponds to F^+, based on the number of vortices present on the airfoil. Consideration of the fully rolled-up vortices (Fig. 25a) indicates that $F^+ \sim 2.2$. Small increases in angle of attack [$\alpha = 2$ deg (Fig. 25b)] produce an asymmetric wake structure with a larger overall transverse width, but the distance between the structures is not affected. Further increases [$\alpha = 4$ deg (Fig. 25c)] produce the same trend, whereas the vortex rollup occurs closer to the trailing edge, and the interstructure distance still remains the same. Up to this angle, the wavelength between the structures does not vary appreciably. As the airfoil approaches incipient stall [$\alpha = 6$ deg (Fig. 25d)], the upper-surface bubble is seen to be shedding into the wake and interacting directly with the vortex shed from the lower surface. This has significant consequences for the wake; namely, formation of the vortex structure now occurs immediately downstream of the airfoil trailing edge, the transverse extent of the wake increases dramatically, while its basic structure remains the same, and the wavelength between structures is approximately doubled. Further α increases to poststall angles dramatically alters the vortex-shedding mechanisms (see Fig. 17).

Forcing the flow at incipient stall ($\alpha = 6$ deg) has significant effects on the wake structure. To illustrate this, flow-visualization photographs are shown for the 5% duty cycle, in which the pulsing frequency was varied from 8 to 54 Hz, corresponding to $F^+ = 0.5$ to 3. Small reductions in C_l, resulting from control (e.g., Fig. 16a) are measured under these conditions, due to the reduction of the bubble size. Forcing at $F^+ = 0.5$ (Fig. 26a) shows a significant effect on the bubble, and a single structure is observed extending approximately $x/c = 25\%$ above the plate's upper surface. It seems that this structure produces two significant effects on the wake; namely, the first rolled-up structure evident immediately downstream of the trailing edge in the baseline case now forms at approximately 1.5 chord lengths downstream of the trailing edge, and instead of regularly spaced structures, the wake is now composed of a larger counterclockwise structure interposed with smaller, mainly clockwise, rotating structures.

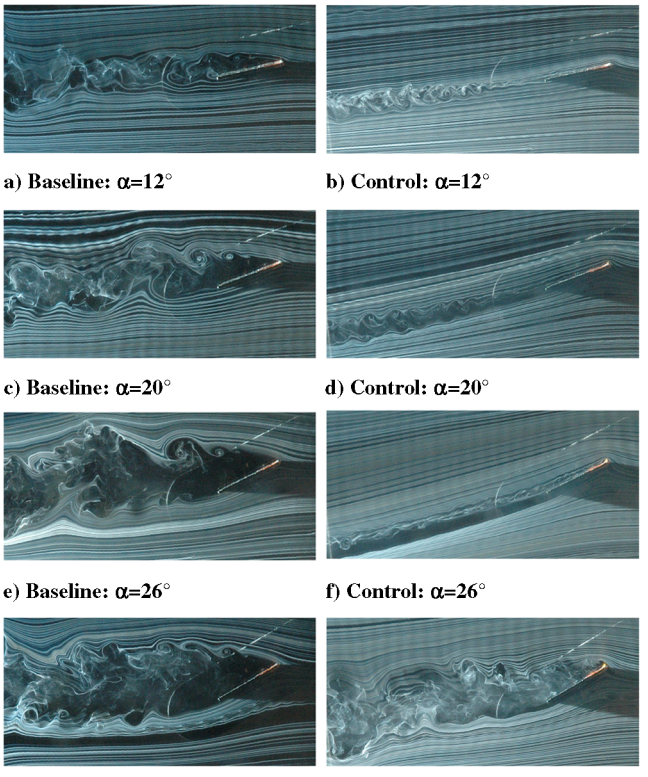

Fig. 23 Flow visualization of baseline and steady control (at 4 kHz and DC = 100%); $Re = 3000$ for increasing angle of attack.

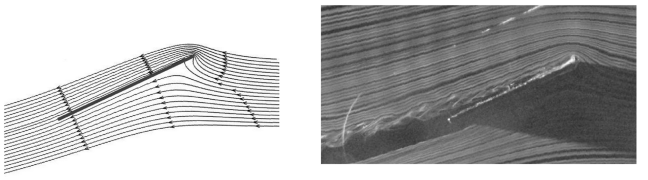

Fig. 24 Streamlines at $\alpha = 26$ deg for a) the potential flow solution around a flat plate and b) steady control (DC = 100% at 4 kHz) generated by means of smoke visualization; $Re = 3000$.

Forcing the flow at incipient stall ($\alpha = 6$ deg) has significant effects on the wake structure. To illustrate this, flow-visualization photographs are shown for the 5% duty cycle, in which the pulsing frequency was varied from 8 to 54 Hz, corresponding to $F^+ = 0.5$ to 3. Small reductions in C_l, resulting from control (e.g., Fig. 16a) are measured under these conditions, due to the reduction of the bubble size. Forcing at $F^+ = 0.5$ (Fig. 26a) shows a significant effect on the bubble, and a single structure is observed extending approximately $x/c = 25\%$ above the plate's upper surface. It seems that this structure produces two significant effects on the wake; namely, the first rolled-up structure evident immediately downstream of the trailing edge in the baseline case now forms at approximately 1.5 chord lengths downstream of the trailing edge, and instead of regularly spaced structures, the wake is now composed of a larger counterclockwise structure interposed with smaller, mainly clockwise, rotating structures.

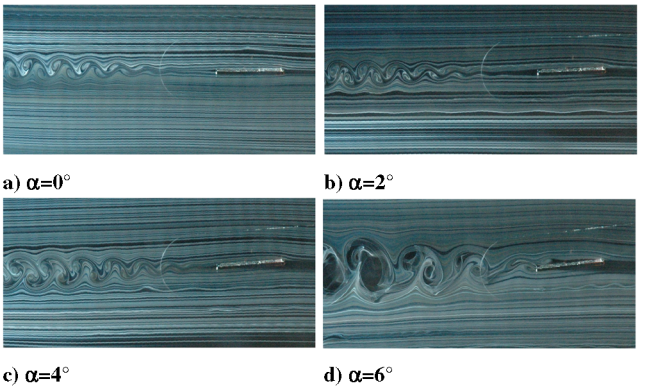

Fig. 25 Flow-visualization photographs of flow over the flat-plate airfoil and in its wake at increasing prestall angles of attack ($Re = 3000$).

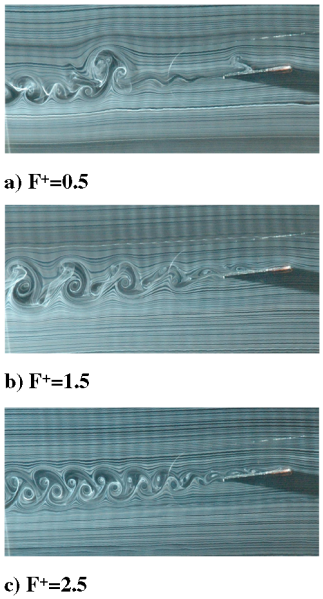

Fig. 26 Flow-visualization photographs of flow over the flat-plate airfoil and in its wake for increasing control reduced frequencies (DC = 5%, $\alpha = 6$ deg, and $Re = 3000$).

The apparent reason for this is that the natural shedding frequency from the upper surface ($F^+ \sim 2.2$) is now regulated to shed at $F^+ = 0.5$, whereas the lower-surface shedding still occurs at $F^+ \sim 2.2$. This results in multiple (~4) clockwise vortices, for which the intervortex spacing is comparable with that at $\alpha = 0$ deg (Fig. 25a) being shed for each counterclockwise vortex, as shown in Fig. 26a. Doubling the forcing frequency [$F^+ = 1.0$ (not shown)] results in the rolled-up wake structure moving closer to the airfoil trailing edge, where each conventional wake structure is now interposed by a single clockwise rotating structure. This is consistent with the preceding explanation in which two clockwise vortices are now shed for each counterclockwise vortex. Further increases in frequency produce multiple vortices on the plate's upper surface. The wake behavior remains consistent with our physical description, and at frequencies comparable with the shedding frequency (e.g., Fig. 26c), the wake regains the structure observed at $0 \text{ deg} \leq \alpha \leq 4$ deg.

V. Conclusions

Active flow control, employing a dielectric barrier discharge plasma actuator, was studied on a flat-plate airfoil and an Eppler E338 airfoil for $3000 \leq Re \leq 20,000$. The following main conclusions were drawn:

1) Pulsed-mode actuation on the flat plate at poststall angles of attack revealed that maximum lift coefficients were generated in the reduced-frequency range of $0.4 < F^+ < 0.6$, with a sharp drop in lift at higher F^+. These data were consistent with NACA 0015 data acquired at 200 times the Reynolds number [7], but differed from the low-Reynolds-number E338 airfoil data [6], which showed a relatively mild dependence on F^+.

2) Duty cycles approximately equal to 5% on the flat plate were found to produce maximum lift, due to the relatively large $\langle C_\mu \rangle$ produced in this DC range. The E338 airfoil lift, however, was nearly insensitive to duty cycle.

3) Actuation produced an increase in $C_{l,\max}$ on the flat plate of up to 0.4 and a similar order of improvements to poststall C_l. These changes did not match those of the E338 (poststall $\Delta C_l > 0.55$), and it was concluded that leading-edge geometry has a profound effect on active flow control efficacy at these Reynolds numbers.

4) Actuation maintained an elevated endurance parameter at significantly higher lift coefficients.

5) Control-based performance enhancements observed on the semispan wing were slightly superior to those observed on the airfoil. This was assumed to be due to tip-vortex modification resulting from actuation near the tip.

6) Actuation in the steady mode produced circulation control at $Re = 3000$ with stall at a 26-deg angle of attack.

7) Control actuation exerted a significant effect on the wake at prestall angles of attack, in which control of the upper-surface bubble shedding produced significant differences in wake spreading and intervortex spacing.

This investigation mainly illustrated the significant effects of DBD actuation at very low flight Reynolds numbers employing both steady and pulsed control. The comparison of different airfoil performance indicators clearly demonstrated the impact of leading-edge detail on the efficacy of active control. Further studies are planned for different airfoil shapes, including the effect of camber, phase-averaged PIV measurements, and different electrode arrangements (cf. [38]).

Acknowledgments

This plasma actuator project was funded by Electrofluidsystems, Ltd. We also gratefully acknowledge the support of C. N. Nayeri as well as the assistance of Y. Kastantin and Y. Singh during the laser Doppler anemometer measurements conducted at the Technical University of Berlin.

References

[1] Mueller, T. J., "Aerodynamic Measurements at Low Reynolds Numbers for Fixed Wing Micro-Air Vehicles," http://www.nd.edu/~mav/belgium.pdf [retrieved Oct. 2007].

[2] Nagel, A., Levy, D. E., and Shepshelovich, M., "Conceptual Aerodynamic Evaluation of Mini/Micro UAV," 44th Aerospace Sciences Meeting and Exhibit, Reno, NV, 2006, AIAA Paper 2006-1261, 9–12 Jan. 2006.

[3] Liang Y., Chung D.-T., and Taya, M., "Bio-Inspired Flapping Actuators Based on Ferromagnetic Shape Memory Alloy Composite and Hybrid Mechanism," *Industrial and Commercial Applications of Smart Structures Technologies*, Proceedings of SPIE, Vol. 6527, Society of Photo-Optical Instrumentation Engineers (International Society for Optical Engineering), Bellingham, WA, 2007. doi:10.1117/12.716231.

[4] Madangopal, R., Khan, Z. A., and Agrawal, S. K., "Biologically Inspired Design of Small Flapping Wing Air Vehicles Using Four-Bar Mechanisms and Quasi-Steady Aerodynamics," *Journal of Mechanical Design*, Vol. 127, No. 4, July 2005, pp. 809–816. doi:10.1115/1.1899690

[5] Raney, D. L., and Slominski, E. C., "Mechanization and Control Concepts for Biologically Inspired Micro Air Vehicles," *Journal of Aircraft*, Vol. 41, No. 6, 2004, pp. 1257–1265.

[6] Roth, J. R., Sherman, D., and Wilkinson, S., "Boundary Layer Flow Control with One Atmosphere Uniform Glow Discharge Surface Plasma," AIAA Paper 1998-0328, 1998.

[7] Corke, T. C., Jumper, E. J., Post, M. L., Orlov, D., and McLaughlin, T. E., "Application of Weakly-Ionized Plasmas as Wing Flow-Control Devices," 40th AIAA Aerospace Sciences Meeting and Exhibit, Reno, NV, AIAA Paper 2002-350, Jan. 14–17, 2002.

[8] Huang, J., Corke, T. C., and Thomas, F. O., "Plasma Actuators for Separation Control of Low-Pressure Turbine Blades," *AIAA Journal*, Vol. 44, No. 1, 2006, pp. 51–57.

[9] Göksel, B., Greenblatt, D., Rechenberg, I., Singh, Y., Nayeri, C. N., and Paschereit, C. O., "Pulsed Plasma Actuators for Separation Flow Control," *Conference on Turbulence and Interactions (TI2006)*, http://www.onera.fr/congres/ti2006/definitivepapers/Goeksel.pdf [retrieved Oct. 2007].

[10] Göksel, B., Greenblatt, D., Rechenberg, I., Nayeri, C. N., and Paschereit, C. O., "Steady and Unsteady Plasma Wall Jets for Separation and Circulation Control," 3rd AIAA Flow Control Conference, San Francisco, AIAA Paper 2006-3686, 5–8 June 2006.

[11] Göksel, B., Greenblatt, D., Rechenberg, I., Kastantin, Y., Nayeri, C. N., and Paschereit, C. O., "Pulsed Plasma Actuators for Active Flow Control at MAV Reynolds Numbers," *Active Flow Control 2006*, edited by R. King, Notes on Numerical Fluid Mechanics and Multidisciplinary Design, Vol. 95, Springer, Berlin, 27–29 Sept. 2006, pp. 42–55.

[12] Greenblatt, D., Göksel, B., Schüle, C. Y., and Paschereit, C. O., "Dielectric Barrier Discharge th Flow Control at Very Low Flight

Reynolds Numbers," *47th Israel Annual Conference on Aerospace Sciences* [CD-ROM], Faculty of Aerospace Engineering, Technion–Israel Inst. of Technology, Haifa, Israel, 21–22 Feb. 2007.

[13] Göksel, B., Greenblatt, D., Rechenberg, I., Bannasch, R., and Paschereit, C. O., "Plasma Flow Control at MAV Reynolds Numbers," 3rd U.S.—European Competition and Workshop on Micro Air Vehicle Systems (MAV07), Toulouse, France, Paper MAV07-PLE1B, Sept. 2007; also available online at http://www.electrofluidsystems.-com/news/Goeksel-et-al-MAV07.pdf.

[14] Göksel, B., Greenblatt, D., Rechenberg, I., and Paschereit, C. O., "Plasma Actuators for Active Flow Control," German Aerospace Congress 2005, Friedrichshafen, Germany, Deutsche Gesellschaft für Luft- und Raumfahrt Paper 2005-210, Vol. 3, pp. 1831–1837, 2005.

[15] Göksel, B., and Rechenberg, I., "Active Flow Control by Surface Smooth Plasma Actuators," *New Results in Numerical and Experimental Fluid Mechanics V, Contributions to the 14th DGLR Symposium of STAB 2004, Bremen*, Notes on Numerical Fluid Mechanics and Multidisciplinary Design, Vol. 92, Springer, New York, 2005, pp. 273–280.

[16] Lachmann,G. V., *Boundary Layer and Flow Control: Its Principles and Application*, Vol 1, Pergamon, New York, 1961.

[17] Moreau, E., "Airflow Control by Nonthermal Plasma Actuators," *Journal of Physics D: Applied Physics*, Vol. 40, 2007, pp. 605–636. doi:10.1088/0022-3727/40/3/S01

[18] Boeuf, J. P., Lagmich, Y., Unfer, Th., Callegari Th., and Pitchford, L. C., "Electrohydrodynamic Force in Dielectric Barrier Discharge Plasma Actuators," *Journal of Physics D: Applied Physics*, Vol. 40, 2007, pp. 652–662. doi:10.1088/0022-3727/40/3/S03

[19] Attinello, J. S., "Design and Engineering Features of Flap Blowing Installations," *Boundary Layer and Flow Control: Its Principles and Application*, edited by G. V. Lachmann, Vol. 1, Pergamon, New York, 1961, pp. 463–515.

[20] Corke, T. C., He, C., and Patel, M. P., "Plasma Flaps and Slats: An Application of Weakly Ionized Plasma Actuators," 2nd AIAA Flow Control Conference, Portland, OR, AAIA Paper 2004-2127, 2004.

[21] Wiltse, J. M., and Glezer, A., "Manipulation of Free Shear Flows Using Piezoelectric Actuators," *Journal of Fluid Mechanics*, Vol. 249, 1993, pp. 261–285. doi:10.1017/S002211209300117X

[22] Greenblatt, D., and Wygnanski, I., "The Control of Separation by Periodic Excitation," *Progress in Aerospace Sciences*, Vol. 36, No. 7, 2000, pp. 487–545. doi:10.1016/S0376-0421(00)00008-7

[23] Seifert, A., Darabi, A., and Wygnanski, I., "Delay of Airfoil Stall by Periodic Excitation," *Journal of Aircraft*, Vol. 33, No. 4, 1996, pp. 691–698.

[24] McLaughlin, D. K., and Tiederman, W. G., "Biasing Correction for Individual Realisation of Laser Anemometer Measurements in Turbulent Flows," *Physics of Fluids*, Vol. 16, 1973, pp. 2082–2088. doi:10.1063/1.1694269

[25] Hussain, A. K. M. F., and Reynolds, W. C., "The Mechanics of an Organized Wave in Turbulent Shear Flow," *Journal of Fluid Mechanics*, Vol. 41, No. 2, 1970, pp. 241–258. doi:10.1017/S0022112070000605

[26] Schmitz, F. W., *Aerodynamik des Flugmodells, Tragflügelmessungen I*, edited by C. J. E. Volckmann Nachf, and E. Wette, Charlottenburg, Berlin, 1942.

[27] Roth, J. R., and Dai, X., "Optimization of the Aerodynamic Plasma Actuator as an Electrohydrodynamic (EHD) Electrical Device," 44th AIAA Aerospace Sciences Meeting and Exhibit, Reno, NV, AIAA Paper 2006-1203, 2006.

[28] Greenblatt, D., and Wygnanski, I., "Effect of Leading-Edge Curvature on Airfoil Separation Control," *Journal of Aircraft*, Vol. 40, No. 3, 2003, pp. 473–481.

[29] Carr, L. W., "Progress in Analysis and Prediction of Dynamic Stall," *Journal of Aircraft*, Vol. 25, No. 1, 1988, pp. 6–17.

[30] Shyy, W., Berg, M., and Ljungqvist, D., "Flapping and Flexible Wings for Biological and Micro Air Vehicles," *Progress in Aerospace Sciences*, Vol. 35, No. 5, 1999, pp. 455–505. doi:10.1016/S0376-0421(98)00016-5

[31] Pornsin-Sirirak, T., Lee, S. W., Nassef, H., Grasmeyer, J., Tai, Y. C., Ho, C. M., and Keennon, M., "MEMS Wing Technology for a Battery-Powered Ornithopter," Thirteenth IEEE International Conference on Micro Electro Mechanical Systems (MEMS '00), Miyazaki, Japan, Inst. of Electrical and Electronics Engineers, Piscataway, NJ, 23–27 Jan. 2000, pp. 799–804.

[32] Maxworthy, T., "The Fluid Dynamics of Insect Flight," *Annual Review of Fluid Mechanics*, Vol. 13, 1981, pp. 329–350. doi:10.1146/annurev.fl.13.010181.001553

[33] Spedding, G. R., and Maxworthy, T., "The Generation of Circulation and Lift in a Rigid Two-Dimensional Fling," *Journal of Fluid Mechanics*, Vol. 165, 1986, pp. 247–272. doi:10.1017/S0022112086003087

[34] Greenblatt D., and Wygnanski, I., "Use of Periodic Excitation to Enhance Airfoil Performance at Low Reynolds Numbers," *Journal of Aircraft*, Vol. 38, No. 1, 2001, pp. 190–192.

[35] Anderson, J. D., *Fundamentals of Aerodynamics*, McGraw–Hill, New York, 1991.

[36] Greenblatt, D., and Washburn, A., "Influence of Finite Span and Sweep on Active Flow Control Efficacy," 25th AIAA Applied Aerodynamics Conference, Miami, FL, AIAA Paper 2007-4275, June 2007.

[37] O'Meara, M. M., and Mueller, T. J., "Laminar Separation Bubble Characteristics on an Airfoil at Low Reynolds Numbers," *AIAA Journal*, Vol. 25, No. 8, Aug. 1987, pp. 1033–1041.

[38] Santhanakrishnan, A., and Jacob, J. D., "Flow Control with Plasma Synthetic Jet Actuators," *Journal of Physics D: Applied Physics*, Vol. 40, 2007, pp. 637–651. doi:10.1088/0022-3727/40/3/S02

N. Chokani
Associate Editor